

Avalanche dynamics in sheared athermal particle packings occurs via localized bursts predicted by unstable linear response

Ethan Stanifer[†] and M. Lisa Manning^{‡*}

Under applied shear strain, granular and amorphous materials deform via particle rearrangements, which can be small and localized or organized into system-spanning avalanches. While the statistical properties of avalanches under quasi-static shear are well-studied, the dynamics during avalanches is not. In numerical simulations of sheared soft spheres, we find that avalanches can be decomposed into bursts of localized deformations, which we identify using an extension of persistent homology methods. We also study the linear response of unstable systems during an avalanche, demonstrating that eigenvalue dynamics are highly complex during such events, and that the most unstable eigenvector is a poor predictor of avalanche dynamics. Instead, we modify existing tools that identify localized excitations in stable systems, and apply them to these unstable systems with non-positive definite Hessians, quantifying the evolution of such excitations during avalanches. We find that bursts of localized deformations in the avalanche almost always occur at localized excitations identified using the linear spectrum. These new tools will provide an improved framework for validating and extending mesoscale elastoplastic models that are commonly used to explain avalanche statistics in glasses and granular matter.

1 Introduction

Can we predict how amorphous materials such as bulk metallic glasses^{1,2}, dense colloidal suspensions³, and foams^{4,5} fail under stress? While most foams and crystalline metals are ductile and fail homogeneously, bulk metallic glasses fail catastrophically via shear bands^{1,6}, despite their otherwise desirable material properties. What microscopic properties generate this macroscopic difference? Such a fundamental description would allow rational material design to control failure mechanisms, such as shear bands and avalanches².

Under small deformations or forces, termed the "pre-yielding regime", amorphous materials respond like elastic solids where the shear stress increases with strain, although small rearrangements can occur in this regime⁷. Above some critical threshold in stress or strain, amorphous materials typically yield macroscopically via irreversible plastic deformations, and the resulting macroscopic stress-strain curve approaches a constant in steady state, with a magnitude that depends on the rate of strain⁷.

However, different materials exhibit vastly different behaviors during this yielding transition⁷. Soft, ductile materials like foams and emulsions yield in a smooth and gradual process as the system begins flow under stress⁸. When brittle materials cross this critical threshold, they tend to yield abruptly and catastrophically via crack, shear band, or avalanche.^{2,8}

Unfortunately, it remains unclear what micro- or meso-scopic features govern this brittle-to-ductile transition. Previous work on athermal avalanches have largely focused on systems under athermal quasistatic shear, where configurations are analyzed before and after the system spanning rearrangements^{9,10}. A few works have also focused on packings sheared under finite strain rate¹⁰⁻¹². These studies evaluate the size, statistics, and/or shape distribution of these avalanches as a function of material properties, often with a focus on the ductility of the initial configuration^{7,10}.

Avalanches in ductile systems are typically not well-organized in space and can occur with relatively little energy imparted to the system. Brittle systems, however, exhibit shear bands. Several studies of avalanches additionally analyze how the shape and size of these rearrangements depend on dynamic features such as strain rate or inertia¹⁰⁻¹³.

Phenomenological work has focused on understanding the transition from ductile to brittle failure in terms of macroscopic system parameters such as composition, temperature, or preparation¹⁴⁻¹⁶. Explanations of this brittle-to-ductile transition have focused on random first order critical points^{15,17} or directed percolation transitions^{18,19}. Recently some authors have used mesoscopic elastoplastic models to investigate the origin of the transition from a brittle-to-ductile behavior^{15,16}. In these models, it is assumed the system is comprised of independent, mesoscopic yielding regions and that the stress to yield x in each region is taken from a specified distribution $P_0(x)$ that captures different preparation protocols. In poorly annealed systems, the mean of $P_0(x)$ is expected to be small, while in well-annealed systems it is large. This hypothesis is strongly supported by work from Patinet et al.²⁰ who explicitly measure local yield stresses, with some assumptions and caveats, in simulated granular systems.

Other models such as Shear Transformation Zone (STZ) and Soft Glassy Relaxation (SGR) also describe localized regions that deform and fail within the glassy systems^{13,21,22}. These models make similar assumptions about the distribution of soft spots or yield stress throughout the system, but they are mean-field in the sense that the yielding of one region effects the stress everywhere else equally instead of via a non-positive elastic kernel. Moreover, in some versions of these models researchers postulate that there can be local diffusion of softness; rearrangements in one location can cause nearby locations to become soft⁸.

At a microscopic level these models assume that plasticity is controlled by "shear transformations", the discrete localized events where a small number of particles rearrange locally, which release the accumulated stress^{22,23}. Similar to elastoplastic models^{16,24}, this implies system-spanning rearrangements occur as sequential bursts of localized motion. An important difference between these models is how defects are coupled dynamically

[†] Department of Physics, University of Michigan, Ann Arbor, Michigan 48109, USA

[‡] Department of Physics and BioInspired Institute, Syracuse University, Syracuse, New York 13244, USA

* To whom correspondence should be addressed: mmanning@syr.edu

during an avalanche. Elastoplastic models couple defects by explicitly quadrupolar elastic stress fields while the STZ/SGR models couple defects via local structural changes and noise. In order to test these predictions for coupling between soft regions during avalanches, we first need a robust method for extracting soft regions from unstable amorphous packings.

Unlike dislocations in crystalline solids, defects in amorphous solids are not easily identified by the local geometry. One way to find soft, defect-like regions is via direct measurements of local yield stress by Patient and collaborators²⁰ discussed above. Additionally, quite a few new techniques have been developed to identify structural indicators that predict plasticity. Some focus on the linear or nonlinear response near an instability^{25–30}, while others use machine learning techniques^{31,32} or identification of high energy motifs³³. Recently, many of these have been compared on the same set of data across the brittle-to-ductile transition, and one conclusion of that work is that structural defect indicators based on linear response are surprisingly predictive³⁴.

Linear response indicators are computed from the hessian: $H = \partial^2 U / \partial u_i \partial u_j$, where U is the potential energy and u_i is the displacements of particle i ³⁵. One such structural indicator is simply a weighted superposition of the lowest energy eigenmodes of the dynamical matrix, or vibrational modes. The resulting field is termed "vibrality"³⁶, or "soft spots" if the field is clustered²⁵. Of course, the lowest energy vibrational mode just before the instability is precisely the initial motion during the avalanche^{25,37}, and the nonaffine displacement field is dominated by these low-energy modes close to the instability, as well^{25,27,34}.

However, structural metrics based on linear response may fail to predict large avalanches because they are computed once before the avalanche, and can not be computing during the avalanche. That is because these methods assume a positive-definite dynamical matrix, but during most of the avalanche dynamics, the Hessian matrix has at least one negative eigenvalue. Therefore, it is obvious to ask whether some of the methods for identifying soft spots in positive-definite Hessians can be extended to Hessians describing unstable systems with one or more negative eigenvalues.

In this manuscript, we develop such extensions and calculate soft spots in order to investigate how they evolve over the course of an avalanche. To understand whether we can really describe avalanches as bursts of localized motions, we also develop a new method for isolating non-affine movements in the D_{min}^2 field¹³ using an extension of persistent homology. This allows us to robustly separate an avalanche into a set of localized rearrangements. Finally, we compare these rearrangements to evolving soft spots to understand how soft spots are coupled to generate the observed dynamics.

These methods may be useful not only for quasistatically sheared athermal systems, but potentially many other unstable systems such as active matter systems, which may be amenable to similar techniques, or thermal systems which are typically not in mechanical equilibrium.

2 Methods

We study bidisperse granular packings. Particles interact with a Hertzian contact potential where the potential energy as a function of distance is given by

$$V(r_{ij}) = \frac{2}{5} \left(1 - \frac{r_{ij}}{r_i + r_j} \right)^{\frac{5}{2}} \quad (1)$$

where r_{ij} is the distance between particle i and j , and r_i and r_j are the radii of particles i and j respectively³⁸. We study 50:50 mixtures of particles with a size ratio of 1:1.4 in order to suppress crystallization³⁹. Two-dimensional systems are initialized with random positions in a square periodic simulation box with equal parts small and large particles. The systems are then instantaneously quenched to zero temperature via FIRE energy minimization⁴⁰.

After the quench process, the systems are strained using Lees-Edwards boundary conditions. We simulate athermal quasistatic shear (AQS) by taking a small shear step and minimizing the total energy of the system using a FIRE minimization algorithm. Since the system is allowed to relax as long as necessary to find an energy minimum after each shear step, this approximates a strain rate that approaches zero in large systems.

Following each strain step, the shear stress of the minimized configuration is measured. If the instantaneous change in shear stress is larger than a specified threshold, which signifies an instability, we use a linear bisection algorithm to identify the precise strain at which the instability occurs⁴¹. Using this procedure, we are able to isolate the system just before and just after an instability corresponding to a particle rearrangement.

Once we have identified a particle rearrangement event, we then wish to simulate the dynamics of that event. In athermal quasistatic shear, the minimum energy states at the end of an avalanche are usually found using fast algorithms, such as conjugate gradient minimization or FIRE, that do not necessarily correspond to realistic dynamics. To maintain physically reasonable dynamics, we instead minimize energy using a computationally expensive steepest descent algorithm with an adaptive timestep. This method is equivalent to a noiseless molecular dynamics simulation in the overdamped limit where the velocity is given by the force with some damping coefficient, which we use to define the natural time unit of the system.

3 Results

3.1 Plastic deformation in avalanches occurs in bursts.

Plasticity in disordered systems is well captured by D_{min}^2 , a measure of the nonaffine motion¹³. D_{min}^2 compares two configurations of a system over a specified radius, in this case five average particle radii:

$$D_{min,i}^2(\vec{X}_1, \vec{X}_2) = \sum_{j:r_{ij} < 5\bar{r}} (\vec{r}_{ij2} - \mathbf{S}\vec{r}_{ij1})^2, \quad (2)$$

where \vec{X}_1 and \vec{X}_2 represent the two configurations being compared, r_{ij} is the distance between particles i and j , \bar{r} is the average particle radius, \vec{r}_{ij1} and \vec{r}_{ij2} are the vectors that separate particles

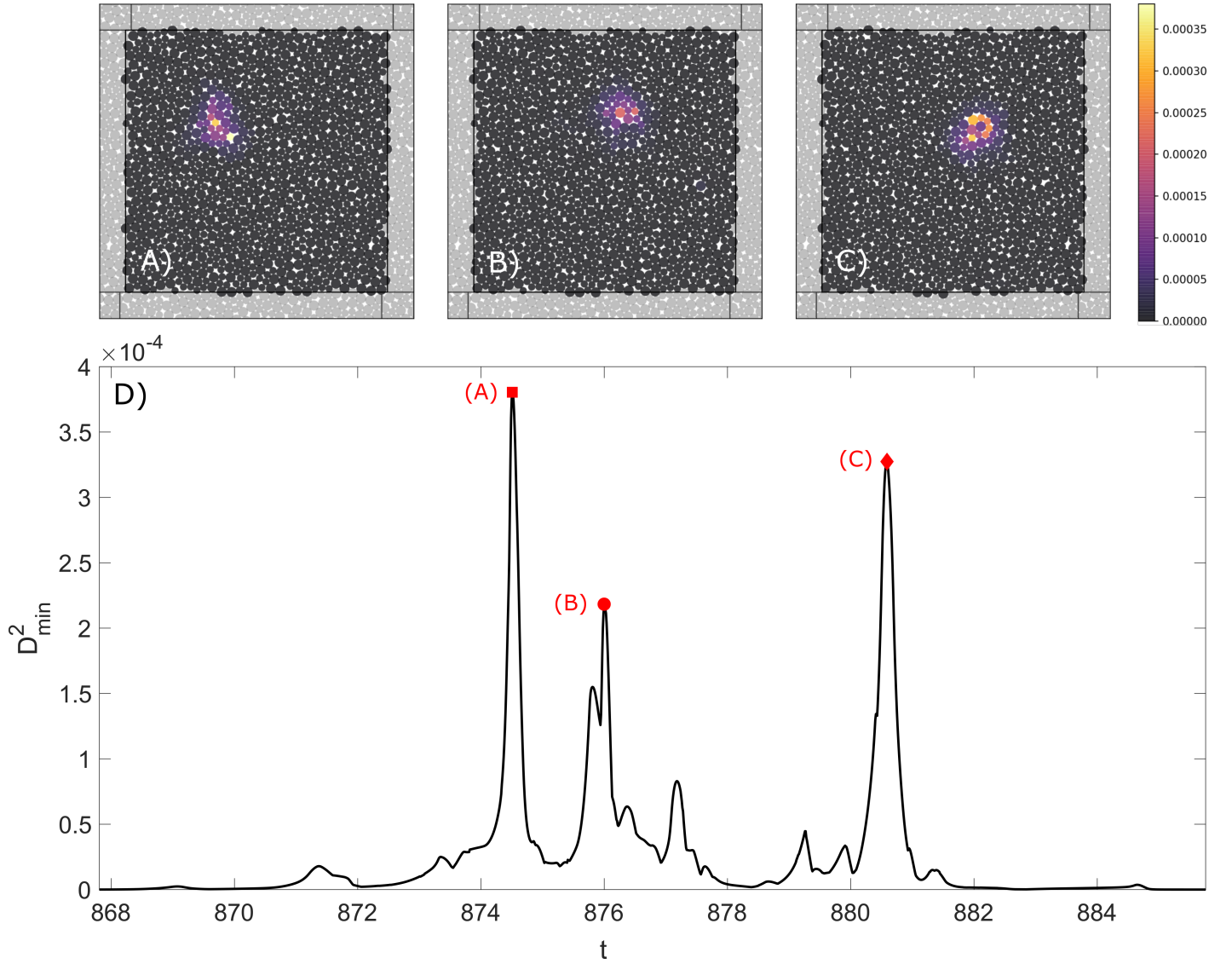


Fig. 1 Sequential snapshots of the D_{min}^2 field are shown in panels (A), (B), and (C). (D) The maximum D_{min}^2 as a function of time for an example avalanche. Red symbols indicate the times at which the snapshots were extracted.

i and j in the first and second configuration respectively, and \mathbf{S} is the best fit affine transformation that minimizes $D_{min,i}^2$.

Our goal is to measure instantaneous plasticity over time. Therefore, we measure D_{min}^2 between two configurations separated by a small time window throughout the minimization. The bursts of localized deformation have a duration on the order of one natural time unit, so we choose to measure the plasticity over a time window, Δt , of 0.2 natural time units to obtain good resolution. We denote the plasticity measured at time t with

$$D_{min,i}^2(t) = D_{min,i}^2\left(\vec{X}\left(t - \frac{\Delta t}{2}\right), \vec{X}\left(t + \frac{\Delta t}{2}\right)\right) \quad (3)$$

where $\vec{X}(t')$ is the configuration at time t' . This measure is a scalar field measured on each particle over space and time. Examples of the D_{min}^2 during one avalanche are shown in Fig. 1 A, B, and C.

As shown in Fig. 1(D), the maximum value of D_{min}^2 exhibits

clear bursts of motion where the maximum value increases by orders of magnitude rapidly and decreases quickly. Furthermore, the D_{min}^2 fields shown in panels (A-C) in Fig. 1 correspond to the peaks of the three largest bursts of motion. These panels illustrate that the location of these bursts of motion are different for each burst.

For each avalanche, $t = 0$ corresponds to the time at which the instability occurs. However, we note that the first burst of localized deformation is often quite delayed. In the example in Fig. 1, the first burst doesn't begin until 868 natural time units after minimization starts. Leading up to that point there is very little motion or activity. This delay occurs because the system begins very near the saddle point instability that triggers rearrangement. Near this saddle point the net force on the system is very small and since the velocity in steepest descent is given by the force, the velocity is also small. It takes time for the system to leave the saddle point behind and approach the time of interest. Similarly,

after all the rearrangements have finished, the system relaxes to a minimum and becomes increasingly slow as it approaches. These build-up and relaxation phases take up the bulk of the time during steepest descent minimization, taking on the order of hundreds or thousands of time units, while the system only rearranges for on the order of tens of time units for the system sizes we study.

3.2 Avalanches can be decomposed into bursts of localized deformation.

It appears that the bursts of localized motion are localized to relatively small groups of particles. To investigate this, we introduce a novel clustering algorithm taking inspiration from persistent homology⁴² and hierarchical density-based clustering methods⁴³.

Our goal is to highlight isolated peaks in the nonaffine motion in this system over space and time to quantify whether the motion during an avalanche occurs in localized bursts. The simplest criteria would be a threshold on the nonaffine motion. However, it is clear that applying a bare threshold to a function could easily lose significant peaks and may not well separate the most active peaks. Furthermore, this kind of clustering is very sensitive to the threshold value which must be determined arbitrarily.

By contrast, persistent homology is a sophisticated analysis method for robust characterization of topological features of a set of data or a function over space. It can be used to characterize the height and spatial extent of topological features like local maxima and minima⁴². This method has been used to quantify the typical heights and sizes of the peaks in a test function and separate them from noise. A schematic diagram of an example test function $\phi(x)$ is shown in Fig. 2(A), and the corresponding standard persistent homology tree diagram is shown in Fig. 2(B), which consists of the height of birth events $\phi(B)$, corresponding to function maxima, and the height of death events $\phi(D)$, corresponding to points where two maxima merge. To separate signal from noise, one can identify a set of criteria to "prune" the leaves of the tree diagram that correspond to maxima that are simply noise fluctuations, as illustrated by the dotted lines for the two highest branches in Fig. 2(B).

For our problem, we must cluster in space and time simultaneously, which requires that we choose how often to sample in time and set a conversion constant, c , between distances in time and distances in space. To ensure good temporal resolution of deformation, we choose a frame rate of 0.01 natural time units. Next, we define a characteristic length scale for the dynamics of interest, which is roughly the length scale of shear transformation zone also used in the D_{min}^2 calculation¹³. In 2D, this is about five particle radii, or $l_{char} = 5\bar{r}$. Similarly, the characteristic timescale should be roughly the time required for a rearrangement of a shear transformation zone, on the order of a natural time unit. Here we use $t_{char} = 0.1$, which is half the $\Delta t = 0.2$ chosen for calculating D_{min}^2 . Then the conversion constant is $c = l_{char}/t_{char} = 50$ in units of natural length over natural time. The distance between two particles in space-time is then given by the usual distance with periodic boundary conditions in space, $d(\vec{x}_i, \vec{x}_j)$, modified by the temporal distance

$$\tilde{d}(i, j) = \sqrt{d^2(\vec{x}_i, \vec{x}_j) + c^2(t_j - t_i)^2}, \quad (4)$$

where \vec{x}_i and t_i are the position and time of particle i .

We next need to develop a criteria for pruning the tree and separating signal from noise. We find that the standard persistent homology method based on persistence (i.e. the distance of the node from the diagonal in the tree diagram), does not efficiently separate signal from noise, and so we improve it using ideas from hierarchical density-based clustering. Specifically, we choose to prune the persistent homology tree based on a threshold for the volume of the identified cluster, where the volume is the sum over the number of particles in the cluster multiplied by the number of frames in the cluster. All leaves with volumes below the volume threshold are pruned.

To identify the optimal threshold, we calculate the relative mutual information between the clusters identified at different volume thresholds, where mutual information is a measure of the amount of information one variable contains about another. The mutual information is constructed by measuring the entropy between datasets I and J given by:

$$M(I, J) = \sum_{x \in I} \sum_{y \in J} p_{x,y} \log_2 \left(\frac{p_{x,y}}{p_x p_y} \right). \quad (5)$$

The relative mutual information between datasets I and J is computed by normalizing by the mutual information by the average self-information between the datasets:

$$m(I, J) = \frac{M(I, J)}{\sqrt{M(I, I) * M(J, J)}}. \quad (6)$$

If there is a good separation between signal and noise in this persistent homology representation, we expect to find a plateau in the mutual information, which indicates that the value of the threshold does not strongly impact the clusters found. In other words, all thresholds th_V in the plateau region are sufficient to separate signal from noise. In Fig. 2(C), we show the relative mutual information between the clusters identified at different size thresholds. We highlight using black lines the region within 5% of the total information. We note that the size of this region varies rapidly with threshold until $th_V \sim 500$, and attains a plateau after that. Therefore, we choose $th_V = 500$, which is the smallest choice of threshold for pruning that separates signal from noise. This minimum cluster volume corresponds to a localized burst of deformation that contains roughly 10 particles and lasts 0.5 natural time units.

In Fig. 3(A), we show a space-time plot of the clusters of non-affine motion, as measured by the D_{min}^2 . Note that this system has periodic boundary conditions in the x - and y - directions, so some of the bursts of localized deformation cross this boundary. These clusters meaningfully highlight nonaffine motion in the system during an avalanche. In Fig. 3(B), we show the nonaffine motion occurs in peaks over time, where the black curve shows the $D_{min,i}^2(t)$ maximized over particles, indicating that avalanches occur in bursts of motion. The localized clusters on this nonaffine motion are well separated in time and space and represent the local maxima as seen in Fig. 3 B, where the clusters clearly highlight the peaks in motion over time.

From the beginning of the first burst of localized deformation to

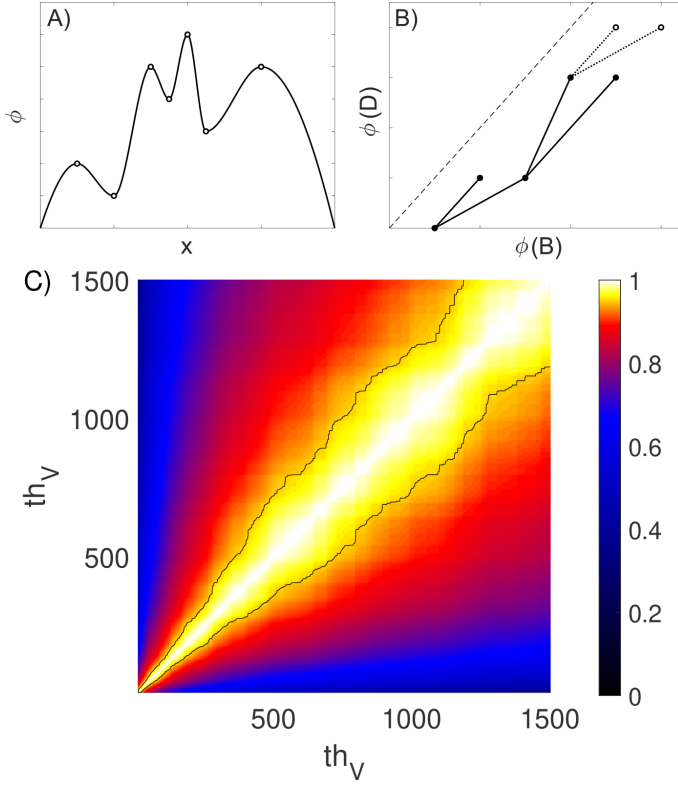


Fig. 2 An extended persistent homology procedure for clustering D_{min}^2 . (A) A schematic diagram of a function $\phi(x)$ to be clustered using persistent homology. (B) The persistence tree for the example field in panel A, where $\phi(B)$ represents the birth height and $\phi(D)$ represents the death height. (C) The relative mutual information between the clusters in our D_{min}^2 identified at different volume thresholds, where the black line represents the region within 5% of the total information.

the end of the last burst, on average the bursts of localized deformation account for $63 \pm 19\%$ of the nonaffine motion while only accounting for $4 \pm 2\%$ of the spacetime volume. These clusters are localized, typically involving less than 100 particles at any given time. The distribution of the spatial extent of the bursts of localized deformation is shown in Fig. 4(A). This distribution has a heavy tail such that the majority of the bursts are relatively small, where the median of this distribution shows half of the bursts of localized deformation involve fewer than 61 particles. Our data appears to be consistent with a log normal distribution, which is represented by the black dashed line in Fig. 4(A).

Additionally, we investigate the duration of these bursts of localized deformation. In Fig. 4(B), we see that the duration of bursts of localized deformation are distributed around unity with a mean value of 2.7 natural time units. Since the duration has a mean that is comparable to the standard deviation but is required to be positive, we hypothesize the distribution of the duration of bursts of localized deformation follows a log-normal distribution, which is shown by the black dashed line and again is consistent with the data.

Perhaps surprisingly, the duration and the size of each burst of localized deformation do not appear to have a strong correlation, as shown in Fig. 4(C). In other words, larger bursts do not

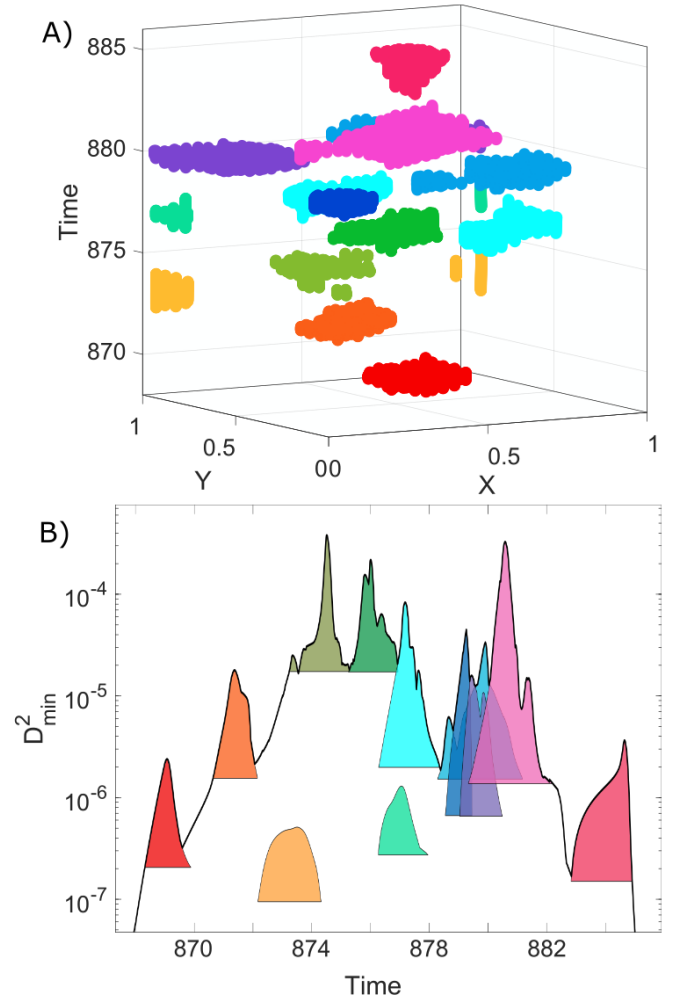


Fig. 3 (A) A space (X,Y) and time plot illustrating the clusters identified by our persistent clustering algorithm in one example avalanche. Colors indicate unique cluster IDs. (B) A plot of the maximum D_{min}^2 over time, where colors identify the D_{min}^2 "meta-peak" associated with each space-time cluster for the example avalanche shown in panel (A).

seem to take longer to complete than smaller bursts of localized deformation.

3.3 Eigenvalue dynamics in unstable systems are highly complex.

The velocity directly follows the force in overdamped dynamics. We choose a damping coefficient of unity such that $\vec{v} = \vec{F}$. Thus, the instantaneous deformation in the system is given by the force.

The change in force is governed by the Hessian matrix, H :

$$\frac{d\vec{F}}{dt} = -H\vec{F}. \quad (7)$$

When we project the force into the eigenbasis of the Hessian, we find a differential equation for the evolution of the force in the direction of each eigenvector:

$$\frac{d}{dt}F_I(t) = -\lambda_I F_I(t), \quad (8)$$

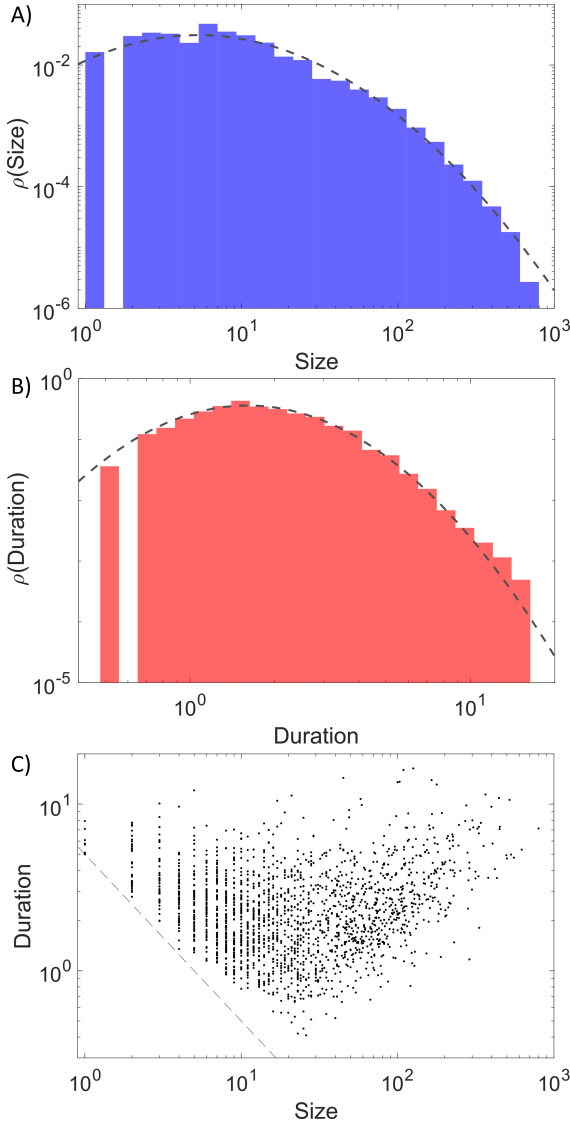


Fig. 4 (A) The distribution of the size of the identified bursts of localized deformation in 100 avalanches. The dashed line shows a log normal distribution. (B) The distribution of the duration of bursts of localized deformation. The dashed line shows a lognormal distribution with the same mean and standard deviation as the duration histogram. (C) The relationship between the duration and the size of the burst of localized deformation identified in 100 avalanches. The dashed line shows the threshold for the spacetime volume of the clustering algorithm.

where $F_I = \langle \vec{F} | \hat{u}_I \rangle$, and λ_I and \hat{u}_I are the I th eigenvalue and associated eigenvector respectively. If we assume the eigenbasis of the Hessian doesn't change quickly relative to the timescale of the force, an assumption we will check later, we can integrate this differential equation to find an exponential function over time:

$$F_I(t) = F_I(0) * e^{-\lambda_I t}. \quad (9)$$

In mechanically unstable systems where the Hessian possesses at least one negative eigenvalue, the force along these unstable directions grows over time, and the rate of growth depends on the magnitude of the associated eigenvalue. If the eigenvalues are large the force quickly tracks the eigenvalue,

and it is therefore tempting to speculate that the deformation field simply follows the most negative eigenvalue, perhaps with near-instantaneous eigenvalue-switching events, where the lowest eigenvalue changes character, due to structural rearrangements and associated contact changes.

In our unstable system, we investigate the dynamic behavior of the eigenvalues of the Hessian during deformation in order to probe the curvature of the energy landscape along the minimization path. If the potential energy landscape was simple we would expect a single negative eigenvalue that becomes positive as the system approaches the energetic minimum. In Fig. 5, we show the lowest ten eigenvalues over the course of an avalanche. This is the same avalanche example shown in Fig 3, and the red and green regions, respectively, correspond to times with bursts of localized deformation with the same color shown in those plots.

Initially, there is only one negative eigenvalue before the main rearrangements occur and, after the entire avalanche is complete, all eigenvalues become positive as the system approaches the minimum, as expected.

One observation is that, unlike in a simple picture of a single saddle point, many eigenvalues can become negative between the initial configuration, near a saddle point, and the final configuration at a local minimum in the energy landscape. As can be seen in the dashed line associated with the right axis in Fig. 5, there can be as many as 5 or 6 negative eigenvalues as the system rearranges. This is indicative of the system passing nearby many saddle points or higher order saddle points during deformation, although our data do not distinguish between these two cases. Another observation is that the eigenvalue dynamics are highly complex, with multiple timescales including very rapid jumps.

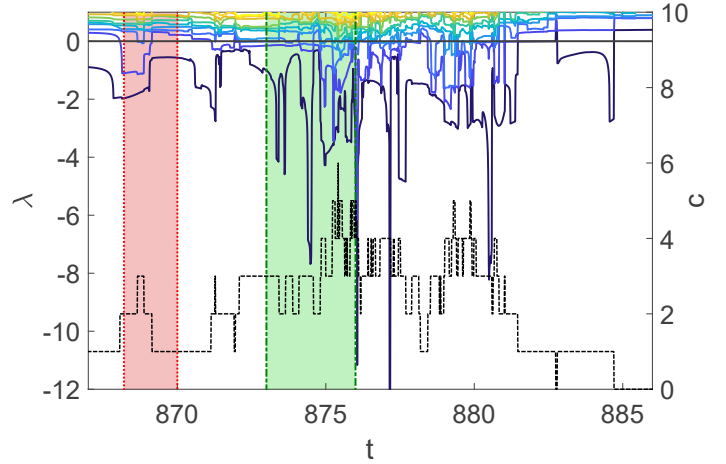


Fig. 5 *Left axis:* The lowest 10 eigenvalues of the Hessian as a function of time for a single avalanche simulation shown by solid lines. *Right axis:* The count, c , of eigenvalues below zero as a function of time shown by dashed line.

To better understand these dynamics and their relationship with the force, we further zoom in on the events associated with the red and green bursts of localized deformation. The red burst is small in magnitude and well-isolated in space and time from other bursts, while the green burst is not.

In Fig. 6 (A), the left (blue) axis quantifies the instantaneous change in the angle $\Delta\theta_{\Psi_{\min}}$ of the eigenvector with the most negative eigenvalue, which we term the "lowest eigenvector" and denote Ψ_{\min} . Spikes in $\Delta\theta_{\Psi_{\min}}$ correspond to "eigenvalue-switching" events, where the lowest eigenvalue changes character rapidly, likely due to a change in the contact network. The right (orange) axis quantifies $\pi/2 - \theta_{F, \Psi_{\min}}$, where $\theta_{F, \Psi_{\min}}$ is the angular difference between the force \mathbf{F} and Ψ_{\min} . The dashed (orange) line corresponds to the difference between the instantaneous force and the lowest eigenvector at the start of the burst, $\Psi_{\min}(t_{\text{ini}})$, while the solid orange line corresponds to the difference between the instantaneous force and the current lowest eigenvector $\Psi_{\min}(t)$. When the force is precisely tracking the eigenvector, this quantity is large (close to $\pi/2$), but it approaches zero if the force is orthogonal to the eigenvector.

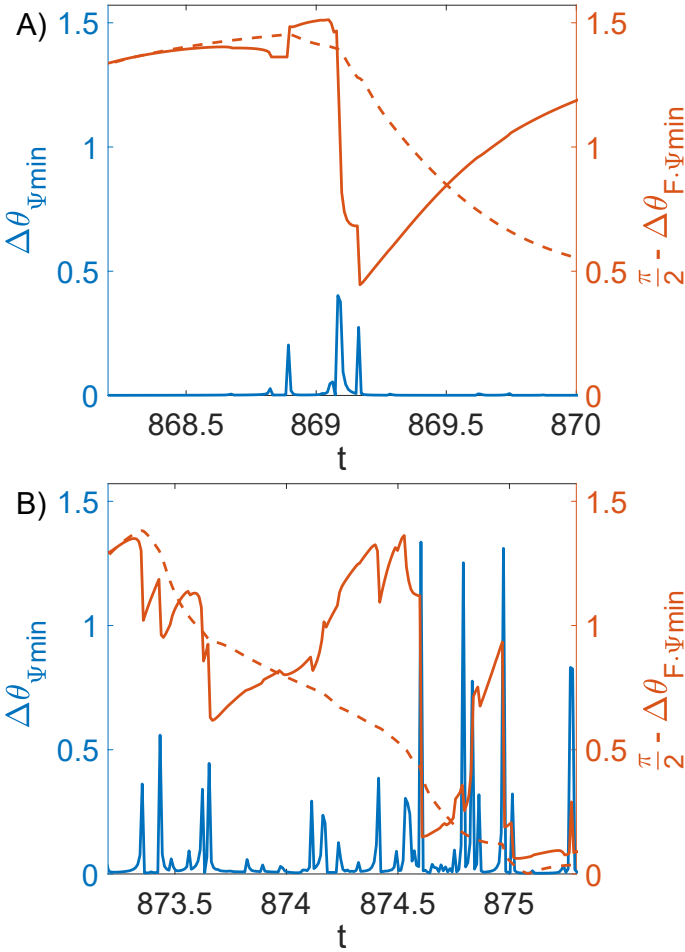


Fig. 6 Left axis (blue) The instantaneous angular change in the lowest eigenmode, $\Delta\theta_{\Psi_{\min}}$, as a function of time. Right axis (orange) The angle of the force with respect to the lowest eigenmode $\Psi_{\min}(t)$, solid; the angle of the force projected into the lowest eigenmode at the beginning of the deformation $\Psi_{\min}(t_{\text{ini}})$, dashed. (A) The eigenvector dynamics during a well-isolated localized burst deformation (the event bounded by the red dotted lines in Fig. 5). (B) The eigenvector dynamics during an event with multiple localized deformations simultaneously (the event bounded in time by the green dashed lines in Fig. 5).

In this simple isolated burst, we see that there are a handful

of rapid, well-separated eigenvalue-switching events. Before the largest such event, the force tracks the lowest eigenvector precisely and the solid orange curve remains close to $\pi/2$. After the largest event, the solid orange curve drops to near zero, indicating that the force is nearly orthogonal to the lowest eigenvector. Then, over a characteristic timescale governed by the magnitude of the eigenvalue, the force begins to track the new lowest eigenvector and the solid orange curve rises again towards $\pi/2$. The dashed line remains low after the eigenvalue switching event, highlighting that the force is no longer tracking the eigenvector that was lowest at the beginning of the burst. Taken together, these data suggest that well-isolated bursts of localized deformation follow our simple sequential picture quite well.

Fig 6(B) shows the same quantities during the green localized burst. First, we notice that there are quite a few rapid changes to the lowest eigenmode over time. Moreover, the timescale between such switching events is smaller than the "force-tracking" timescale associated with the magnitude of the eigenvalue, and so the force almost never matches the lowest eigenvector, as the solid orange curve representing $\pi/2 - \theta_{F, \Psi_{\min}}$ drops and rises several times and approaches zero by the end of the burst. Since these more complex events are quite common, it is clear that the lowest eigenmode is not a good predictor of deformation. This raises the question: are there other indicators based on linear response that would be more stable and therefore more predictive during an avalanche?

3.4 Soft spots can be identified from a superposition of lowest eigenvalues

As there are rapid changes to the lowest eigenmodes, rather than measuring the overlap with each mode individually, we compute a field similar to the vibrality³⁶ over space and time. Vibrality, Ψ , quantifies the susceptibility of particle motion to infinitesimal thermal fluctuations in the limit of zero temperature and is proportional to the Debye-Waller factor. Ψ is defined as:

$$\Psi = \sum_{k=1}^{dN-d} \frac{|\Psi_k|^2}{\omega_k^2}, \quad (10)$$

where the sum runs over the entire set of eigenvectors Ψ_k with frequency ω_k .

To improve performance, we made some alterations to the standard vibrality. First, as computing the full sum over the entire set of eigenvectors at every time step is computationally intensive, we computed the partial vibrality sums over the k^* modes with the lowest eigenvalues, for varying k^* . For stable Hessians and for our system size of interest, we found a partial sum over the lowest eight eigenmodes approximates the true vibrality to within 98%. We expect the number of modes needed to capture the salient features of the structure to increase linearly with system size, though we reserve this for future work.

Second, in the standard vibrality indicator, individual modes are comprised of phonons hybridized with quasi-localized excitations. To remove the phonons, we first compute the non-affine field of each eigenmode by applying the D_{\min}^2 algorithm on each eigenvector as if it were a displacement field, with the same

lengthscale used to quantify deformation, five average particle radii. Third, because the eigenvalues for unstable Hessians are both positive and negative, and therefore the frequency is not well-defined, we remove the weighting with frequency in Eq. 10. We then calculate a new vibrality-like metric, which we term non-affine vibrality and denote $\tilde{\Psi}$, as the magnitude of the unweighted sum of the non-affine field associated with the eight lowest eigenmodes of the Hessian. This can be quickly computed at each timepoint t during a steepest descent minimization routine, as it requires only a partial diagonalization of the Hessian, and captures quasi-localized excitations in the eigenmodes of unstable Hessians.

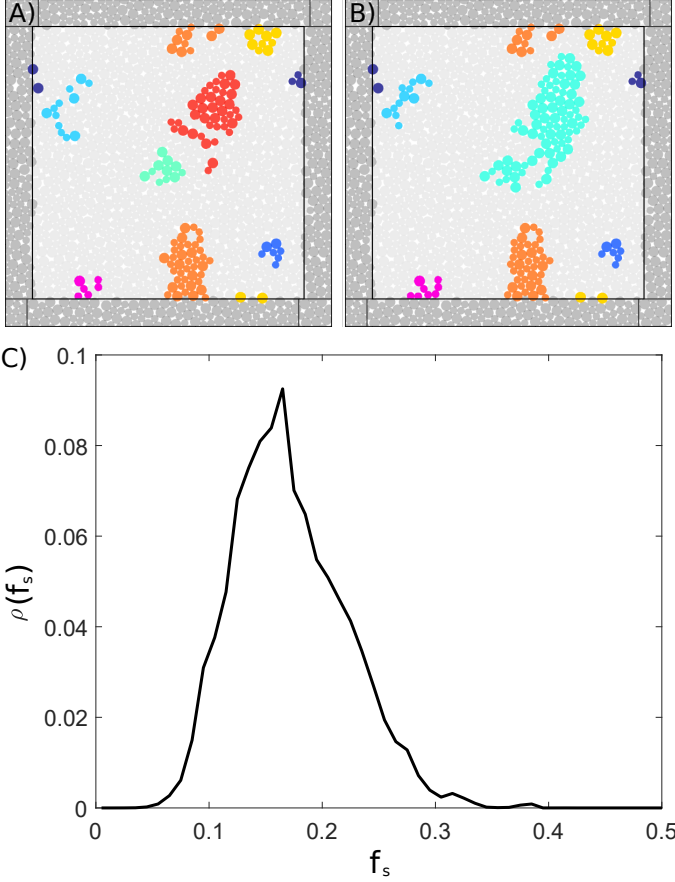


Fig. 7 (A) The clustered soft spots identified in a single time frame, with periodic boundary conditions in space. Colors index distinct clusters. (B) Soft spots identified one frame later. (C) Probability distribution ρ of the fraction of the system f_s labeled soft in each frame.

Having identified the non-affine vibrality $\tilde{\Psi}$ as an efficient structural indicator field for Hessians with negative eigenvalues, we next seek to cluster the field into "soft spots" that can be directly compared with bursts of localized deformations. We found that we were unable to identify soft spots in space and time using the same persistent clustering algorithm used to compute the bursts of localized deformation. This is because while the localized bursts of deformation possess relatively well-defined characteristic length and timescales (see Fig 4), we observe that soft spots exhibit a very large variation in time: some are very short-lived

while others remain for the length of the avalanche. This means there is no choice of volume threshold that separates noise from signal in the persistent homology diagrams.

Although there is no characteristic timescale for soft spots, there is a clear length scale. Therefore, we first use the persistent clustering algorithm to cluster $\tilde{\Psi}$ as a function of space only at each time slice. In Fig. 7 A, we show a snapshot of these space-only clusters at a particular time. In Fig. 7 B, we show the identified clusters at the next time step. Note that the soft spots near the center of the first frame are joined together in the second frame. To determine how to group these space-only clusters in time, we compute the relative mutual information between space-only clusters in adjoining time frames. We expect that spots with large mutual information across time should be grouped together, and those with low information should not. To determine an information threshold, we analyze the mutual information probability distribution for simple events where a soft spot in one frame overlaps with two in another frame, shown in Fig. 8. We find that the median value for these types of events is 0.25, and so we adopt that as a threshold for all events. In the example shown in 7(A) and (B), the upper right overlapping space-only cluster has large enough mutual information to be identified with the space-only cluster in 7(B). This procedure generates from the field $\tilde{\Psi}$ a discrete set of space-time clusters which we term "soft spots". Fig 7(C) is a histogram of the fraction of the system that is labeled as a soft spot in each time step across 150 avalanches, illustrating that our procedure labels about 10-25% of the system as soft spots, which is consistent with previous methods²⁵.

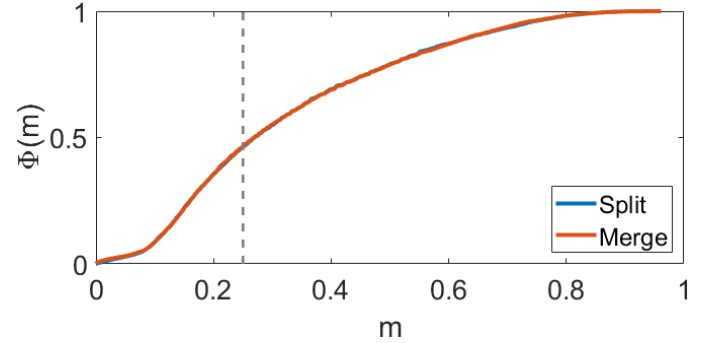


Fig. 8 The cumulative distribution Φ of the relative mutual information between soft spots identified in each time frame separated by the time window of 0.1 natural time units or less averaged over 180 avalanches. These overlaps are separated into cases where the soft spot splits into two soft spots (Split) and where two soft spots merge into one (Merge) which have nearly identical distributions.

3.5 Bursts of localized deformation occur at dynamically changing soft spots

To understand how soft spots correlate with bursts of localized deformation, we study the mutual information between these fields⁴⁴. Specifically, we use a normalized form of the mutual information called the proficiency, which measures how well each soft spot predicts the spatio-temporal location of each burst of

localized deformation:

$$\chi_{IJ} = \frac{M(I, J)}{H(I)}, \quad (11)$$

where $M(I, J)$ is the mutual information between soft spot J and burst of localized deformation I and $H(I)$ is the information measure of the burst of localized deformation I .

We use a modified form of the mutual information between two discrete fields computed as

$$M(I, J) = \sum_{x \in [I, \sim I]} \sum_{y \in [J, \sim J]} p_{x,y} \log_2 \left(\frac{p_{x,y}}{p_x p_y} \right) \Theta(p_{I,J} - p_I p_J), \quad (12)$$

where x is the discrete field of the burst of localized deformation, y is the discrete field of soft spots, and p_x , p_y and $p_{x,y}$ are the probabilities that an arbitrary point in the discrete fields is x in the discrete field formed from the bursts of localized deformation, or y in the soft spot field, or both, respectively. The Heaviside-step function in this definition gives positive information if the overlap between I and J is greater than the expected and negative if X is better correlated to the complement of J . The self-information, $H(I)$, is given by the mutual information with itself, $H(I) = M(I, I)$.

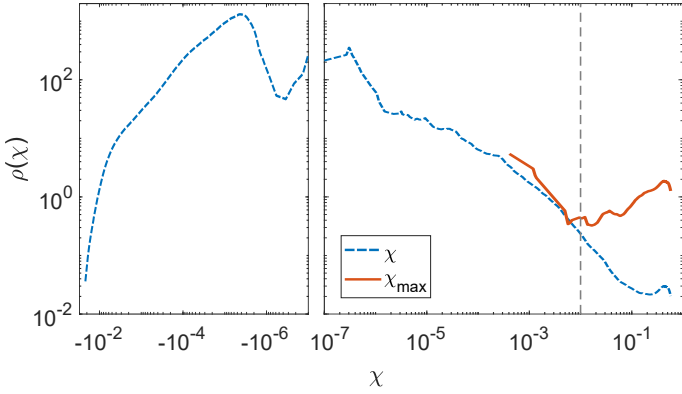


Fig. 9 Probability distribution function ρ of proficiency χ between all bursts of localized deformation and all soft spots (blue dashed line), and the maximum proficiency for each burst of localized deformation (red solid line), from 180 avalanches.

The proficiency is near unity when the spatial location of a soft spot overlaps very well with the spatial location of a burst of localized deformation and occurs at the same time. If the proficiency is very near zero, then the soft spot and the burst of localized deformation have little to no overlap in space and time. The probability distribution function for the proficiencies between all soft spots and bursts of localized deformation is shown by the blue dashed line in Fig. 9. The vast majority of proficiencies are very small or negative, indicating that as expected, most soft spots do not overlap with a plastic event at a given instant in time. In contrast, the maximum proficiency for each burst of localized deformation, shown by the solid red line in Fig. 9, exhibits a bi-modal distribution. The peak at high χ indicates a real overlap between a soft spot and a burst of deformation, while the peak at low χ is consistent with background noise. Therefore, we define the threshold for overlap at the minimum between these two peaks ($\chi = 0.01$),

shown by the vertical dashed line in Fig. 9.

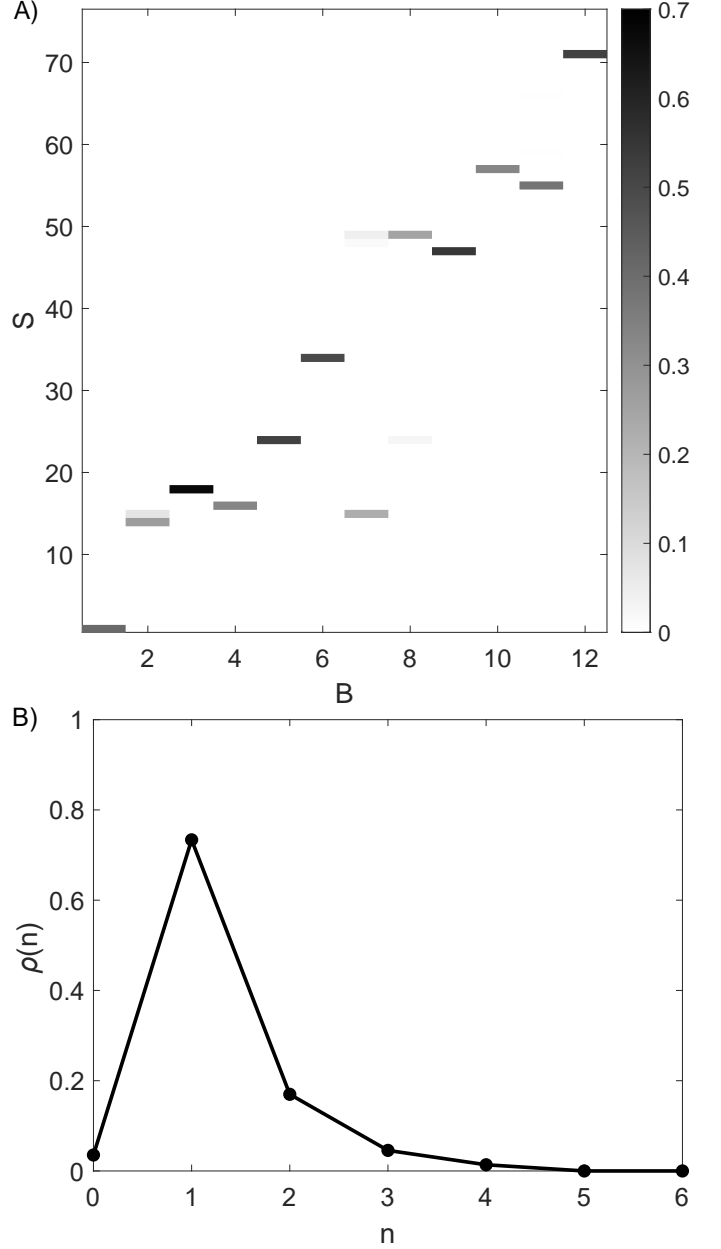


Fig. 10 (A) Overlap between 76 identified soft spots and 12 bursts of localized deformation in a single avalanche. The grayscale colormap indicates the proficiency χ between each soft spot, indexed by S in order of start time, and each burst of localized deformation indexed by B in order of start time. **(B) Number of soft spots associated with a single burst of localization.** The probability distribution ρ of bursts of localized deformation that overlap (possess a proficiency $\chi > 0.01$) with n soft spots across 180 avalanches, indicating that most bursts are associated with one soft spots, though a few are associated with 2 or more.

Fig. 10(A) illustrates the relationship between bursts of deformation and soft spots across a single avalanche. Soft spots are indexed by an integer S in order of their start times, and bursts are similarly indexed by an integer B . The colormap indicates the proficiency between each soft spot and a burst of localized information. This example highlights several features that are

common to avalanches we studied: i) almost all bursts of deformation are associated with at least one soft spot – in this example, all bursts of localized deformation have greater than 1% correlation with at least one soft spot, ii) a small number of bursts are associated with more than one soft spot, iii) many soft spots are not involved at all throughout the entire avalanche, iv) some soft spots show up in more than one burst (i.e. those spots rearrange more than once). To get a better idea of the statistics of these features across multiple examples, Fig. 10(B) shows the fraction of bursts of localized deformation that have an overlap (a proficiency greater than the threshold 0.01) with n soft spots. Only 3.5% of bursts do not overlap with a predicted soft spot, and the majority overlap with one soft spot. This data is consistent with the hypothesis that bursts of localized deformation occur when a structural defect, or soft spot, reaches its yield stress and deforms.

Importantly, many of the soft spots we identify are not present at the start of the avalanche; they appear instead later in the avalanche as a result of the avalanche dynamics. Figure 11 shows the distribution of soft spot start times normalized by the total duration of the avalanche, averaged over 180 avalanche trajectories. While 13% of the soft spots already exist in the mechanically stable state before the avalanche starts, illustrated by the peak on the left-hand side of Fig.11, the remaining distribution is relatively flat, suggesting that soft spots are equally likely to form at any time during the remainder of the avalanche.

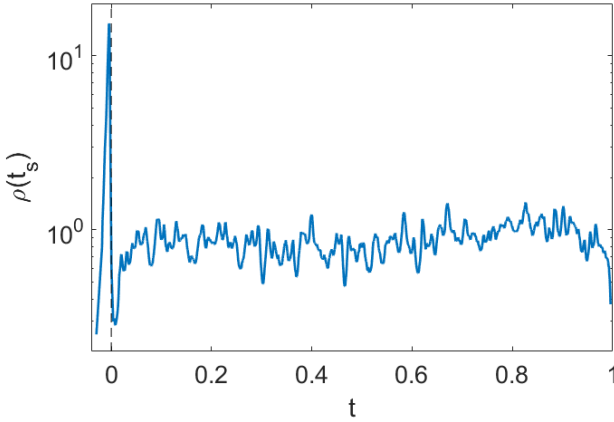


Fig. 11 The distribution ρ of start times (t_s) for soft spots throughout the avalanches where they appear. The start time is normalized such that the instability that triggers the avalanche is occurs at $t = 0$ while the avalanche ends and the system finds a new stable state at $t = 1$.

4 Discussion and Conclusions

In this manuscript, we studied the overdamped dynamics of avalanches in athermal disordered particle packings under applied shear. Using a set of new persistent-homology-based clustering algorithms, we find that the plastic motion in avalanches generally occurs as sequential bursts of localized deformation. This observation is consistent with elastoplastic theories that explicitly predict avalanches to occur as a sequence of triggered localized rearrangements.

Using the normal modes of the Hessian, we probe the curvatures of the unstable system. One important observation is that there are multiple negative eigenmodes that exchange character extremely rapidly – on timescales quite a bit shorter than even those localized bursts of deformation. Therefore, the lowest eigenmode is not predictive of the deformation field in such avalanches. Instead, we develop a vibrality-like structural indicator, $\tilde{\Psi}$ that is quick to compute, and we cluster this structural indicator field into discrete soft spots that can be directly compared with bursts of localized deformation.

We find that bursts of localized deformation almost always occur at soft spots predicted by our structural indicator. In large avalanches, some of these soft spots are not in the low-energy spectrum at the beginning of the instability, and arise due to the dynamics of the avalanche itself. We find that some bursts are associated with multiple soft spots, and that the same soft spot can sometimes appear in two different bursts, indicating that the same spot rearranges more than once during a single avalanche.

This initial study develops a set of tools that could be broadly useful for analyzing dynamics and structure during avalanches in computer-generated glasses, potentially addressing many long-standing questions in the field. One important question is whether a rearranging defect triggers the next defect via a simple elastic kernel, as proposed in elasto-plastic theories, via diffusion of structural or effective-temperature like variables, as proposed in Soft Glassy Rheology²² and Shear Transformation Zone¹³ theories, or perhaps a non-trivial combination of such effects⁴⁵. By studying how these bursts of localized deformation are coupled in space and time, it should be possible to determine whether they are consistent with elastic propagation at speed set by the elastic moduli. Moreover, it may be possible to determine how the newly formed soft spots are correlated with deformation and determine if that is consistent with theories that postulate diffusion of structural information.

This study has focused on two-dimensional disc packings generated via infinite temperature quench, as visualizing structural defects and their evolution over time is much easier in 2D than 3D. However, all of the techniques developed here should be fairly straightforward to extend to 3D sphere packings. In addition, systems prepared via infinite temperature quench are highly ductile and do not exhibit localized shear bands or large stress drops at the yielding transition. Therefore, it will be very interesting to use these new tools to study avalanches in systems that are brittle and where the avalanche is highly localized in space.

Although these methods have been applied to relaxing athermal disordered systems, other unstable systems could also be analyzed using these tools. For instance, studies of the structural evolution of packings in the presence of thermal fluctuations have focused on the inherent, or energy minimized, states or on free-energy minimized configurations. Similarly, studies of active systems, such as crowds of humans or dense packings of driven colloidal particles, have relied on structural evaluations of mechanically stable reference states. In both cases, instantaneous evaluation of the structure of these mechanically unstable systems was not available. It will be interesting to see if the unstable structural indicators we identify in this work are also predictive of the

dynamics there.

5 Acknowledgements

We thank Peter Morse for useful discussions. M.L.M and E.M.S. acknowledge support from NSF-DMR-1951921 and Simons Foundation Grant No. 454947. M.L.M acknowledges additional support from Simons Foundation 446222, and E.M.S. from MURI N00014-20-1-2479.

Notes and references

- 1 W.-H. Wang, C. Dong and C. Shek, *Materials Science and Engineering: R: Reports*, 2004, **44**, 45–89.
- 2 C. SCHUH, T. HUFNAGEL and U. RAMAMURTY, *Acta Materialia*, 2007, **55**, 4067–4109.
- 3 P. Schall, D. A. Weitz and F. Spaepen, *Science*, 2007, **318**, 1895–1899.
- 4 J. Lauridsen, M. Twardos and M. Dennin, *Physical Review Letters*, 2002, **89**, 098303.
- 5 D. Bonn, M. M. Denn, L. Berthier, T. Divoux and S. Manneville, *Reviews of Modern Physics*, 2017, **89**, 035005.
- 6 Y. Zhang and A. L. Greer, *Applied Physics Letters*, 2006, **89**, 071907.
- 7 C. E. Maloney and A. Lemaître, *Physical Review E*, 2006, **74**, 016118.
- 8 A. Nicolas, E. E. Ferrero, K. Martens and J.-L. Barrat, *Reviews of Modern Physics*, 2018, **90**, 045006.
- 9 A. Lemaître and C. Caroli, *Physical Review Letters*, 2009, **103**, 065501.
- 10 K. M. Salerno, C. E. Maloney and M. O. Robbins, *Physical Review Letters*, 2012, **109**, 105703.
- 11 A. Nicolas, J. Rottler and J.-L. Barrat, *The European Physical Journal E*, 2014, **37**, 1–11.
- 12 A. E. Lagogianni, C. Liu, K. Martens and K. Samwer, *The European Physical Journal B*, 2018, **91**, 1–5.
- 13 M. Falk and J. Langer, *Physical Review E*, 1998, **57**, 7192.
- 14 A. Nicolas, E. E. Ferrero, K. Martens and J.-L. Barrat, 2017.
- 15 M. Ozawa, L. Berthier, G. Biroli, A. Rosso and G. Tarjus, *Proceedings of the National Academy of Sciences*, 2018, **115**, 6656–6661.
- 16 M. Popović, T. W. J. de Geus and M. Wyart, *Physical Review E*, 2018, **98**, 040901.
- 17 P. K. Jaiswal, I. Procaccia, C. Rainone and M. Singh, *Physical review letters*, 2016, **116**, 085501.
- 18 G. P. Shrivastav, P. Chaudhuri and J. Horbach, *Physical Review E*, 2016, **94**, 042605.
- 19 A. Ghosh, Z. Budrikis, V. Chikkadi, A. L. Sellerio, S. Zapperi and P. Schall, *Physical review letters*, 2017, **118**, 148001.
- 20 S. Patinet, D. Vandembroucq and M. L. Falk, *Physical Review Letters*, 2016, **117**, 045501.
- 21 M. L. Manning, J. S. Langer and J. M. Carlson, *Physical Review E*, 2007, **76**, 056106.
- 22 P. Sollich, *Molecular Gels*, Springer, 2006, pp. 161–192.
- 23 H. J. Barlow, J. O. Cochran and S. M. Fielding, *From ductile to brittle yielding in amorphous materials*, 2019.
- 24 M. Ozawa, L. Berthier, G. Biroli, A. Rosso and G. Tarjus, *Proceedings of the National Academy of Sciences*, 2018, **115**, 6656–6661.
- 25 M. L. Manning and A. J. Liu, *Physical Review Letters*, 2011, **107**, 108302.
- 26 J. Zylberg, E. Lerner, Y. Bar-Sinai and E. Bouchbinder, *Proceedings of the National Academy of Sciences*, 2017, **114**, 7289–7294.
- 27 S. Wijtmans and M. L. Manning, *Soft Matter*, 2017, **13**, 5649–5655.
- 28 J. Ding, S. Patinet, M. L. Falk, Y. Cheng and E. Ma, *Proceedings of the National Academy of Sciences*, 2014, **111**, 14052–14056.
- 29 L. Gartner, E. Lerner et al., *SciPost Phys*, 2016, **1**, 016.
- 30 D. Richard, G. Kapteijns, J. A. Giannini, M. L. Manning and E. Lerner, *Physical Review Letters*, 2021, **126**, 015501.
- 31 S. S. Schoenholz, E. D. Cubuk, D. M. Sussman, E. Kaxiras and A. J. Liu, *Nature Physics*, 2016, **12**, 469–471.
- 32 V. Bapst, T. Keck, A. Grabska-Barwińska, C. Donner, E. D. Cubuk, S. S. Schoenholz, A. Obika, A. W. R. Nelson, T. Back, D. Hassabis and P. Kohli, *Nature Physics*, 2020, **16**, 448–454.
- 33 H. Tong and H. Tanaka, *Physical Review X*, 2018, **8**, 011041.
- 34 D. Richard, M. Ozawa, S. Patinet, E. Stanifer, B. Shang, S. A. Ridout, B. Xu, G. Zhang, P. K. Morse, J.-L. Barrat, L. Berthier, M. L. Falk, P. Guan, A. J. Liu, K. Martens, S. Sastry, D. Vandembroucq, E. Lerner and M. L. Manning, *Physical Review Materials*, 2020, **4**, 113609.
- 35 W. G. Ellenbroek et al., *Response of granular media near the jamming transition*, Leiden Institute of Physics, Institute-Lorentz for Theoretical Physics, Faculty of Science, Leiden University, 2007.
- 36 H. Tong and N. Xu, *Phys. Rev. E*, 2014, **90**, 010401.
- 37 J. Rottler, S. S. Schoenholz and A. J. Liu, *Physical Review E*, 2014, **89**, 042304.
- 38 K. L. Johnson and K. L. Johnson, *Contact mechanics*, Cambridge university press, 1987.
- 39 C. S. O'Hern, L. E. Silbert, A. J. Liu and S. R. Nagel, *Physical Review E*, 2003, **68**, 011306.
- 40 E. Bitzek, P. Koskinen, F. Gähler, M. Moseler and P. Gumbsch, *Physical Review Letters*, 2006, **97**, 170201.
- 41 M. S. van Deen, J. Simon, Z. Zeravcic, S. Dagois-Bohy, B. P. Tighe and M. van Hecke, *Physical Review E*, 2014, **90**, 020202.
- 42 H. Edelsbrunner and J. Harer, *Persistent homology—a survey*, 2008, <https://doi.org/10.1090/conm/453/08802>.
- 43 R. J. Campello, D. Moulavi and J. Sander, *Pacific-Asia conference on knowledge discovery and data mining*, 2013, pp. 160–172.
- 44 J. White, S. Steingold and C. Fournelle, *Proceedings of Interface 2004*, 2004.
- 45 G. Zhang, S. Ridout and A. J. Liu, *arXiv preprint arXiv:2009.11414*, 2020.